physica status solidi b
www.pss-b.com

Check for updates

Limiting Damage to 2D Materials during Focused Ion Beam Processing

*Anton Bay Andersen, Abhay Shivayogimath, Tim Booth, Shima Kadkhodazadeh, and Thomas Willum Hansen**

2D materials are by definition just a few atomic layers thick. They are therefore ideal samples for transmission electron microscopy, in the plan-view geometry. However, 2D materials are typically placed or grown on substrates, which in some cases requires analysis to be performed on cross sections. In this case focused ion beam preparation is often the technique of choice for producing thin lamellae, but damage to the surface of 2D material during imaging and milling must be mitigated. Herein, it is demonstrated that the typically applied electron beam-assisted deposition of platinum and carbon prior to milling does not provide sufficient protection, and results in significant damage. Instead, it is found that arc-evaporated carbon—deposited with a standard carbon coater designed for scanning electron microscopy (SEM) samples—can provide sufficient protection, enabling cross-sectional analysis without detectable damage to monolayer or bilayer samples subsequently prepared by standard focused ion beam preparation procedures.

1. Introduction

Whether grown by chemical vapor deposition (CVD), exfoliated, and transferred or in a final device, 2D materials are often supported by a substrate. For these structures, cross-sectional samples offer a direct way of investigating the number of layers, the morphology, the crystal structure, and interfaces using (scanning) transmission electron microscopy ((S)TEM). Despite their inherent electron transparency in plan-view, (S)TEM investigation of 2D materials in cross section requires extensive thinning and polishing. Focused ion beam (FIB) milling and lift out of micron size lamellae to TEM compatible grids inside the FIB chamber offer many advantages for the preparation of samples for substrate-bound structures of 2D materials on a substrate. It allows for the rapid preparation of samples from specific selected regions and is highly versatile in terms of the types of materials that can be prepared. Such versatility has required efforts to understand and reduce FIB-induced damage by developing specific milling recipes.[1–5] As an example, FIB can be used to prepare structures after growth or after patterning/contacting for (S)TEM analysis.[6–8] Surface damage introduced during FIB preparation can often be limited to a depth range of few nanometers either by depositing protective layers prior to milling or by adjusting the milling parameters.[9–15] This is sufficient in cases, where the surface atoms are not of explicit interest, such as examination of a metal contact to a 2D material.[7] In cases where the 2D material is the very top layer, as for CVD-grown 2D materials, hardly any damage from the FIB milling can be tolerated. This work shows that arc-evaporated carbon—performed with a standard carbon coater designed for scanning electron microscopy (SEM) samples—provides sufficient protection, enabling cross-sectional analysis of 2D materials with no detectable damage to monolayer or bilayer samples. Furthermore, it is shown that electron beam-assisted deposition of platinum produces surface damage to gold surfaces with a depth greater than the typical thickness of typical 2D materials.

A. B. Andersen, Dr. S. Kadkhodazadeh, Dr. T. W. Hansen
DTU Nanolab
Technical University of Denmark
Fysikvej, Building 307, 2800 Lyngby, Denmark
E-mail: thwh@dtu.dk

Dr. A. Shivayogimath, Dr. T. Booth
DTU Physics
Technical University of Denmark
Fysikvej, Building 309, 2800 Lyngby, Denmark

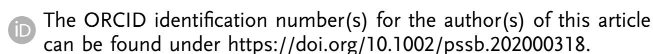
The ORCID identification number(s) for the author(s) of this article can be found under https://doi.org/10.1002/pssb.202000318.

DOI: 10.1002/pssb.202000318

2. Results and Discussion

Cross sections of five different sample types are studied by (S) TEM here. All five lamellae were made with the same FIB preparation procedure. A full description of used materials and procedures of all samples can be found in Section 4, and a sketch of the layered structure is shown in Figure S1, Supporting Information. We note here that electron beam-deposited platinum is not pure platinum, but a mixture of amorphous carbon and platinum particles with a high carbon content.[16,17] Therefore, the major difference between samples with arc-evaporated carbon and electron beam-deposited platinum top layers is not the material that constitutes the layer. It is the deposition technique used to deposit the layer, whether this is by condensation of evaporated carbon during arc-discharge, or by electron-induced CVD of a metal organic precursor.

Figure 1 shows a comparison of high-resolution transmission electron microscope (HRTEM) images of the pure gold surfaces of samples 1 and 2. They are used to compare the damage done by the two methods without the added effect of a 2D material

 © 2020 Wiley-VCH GmbH

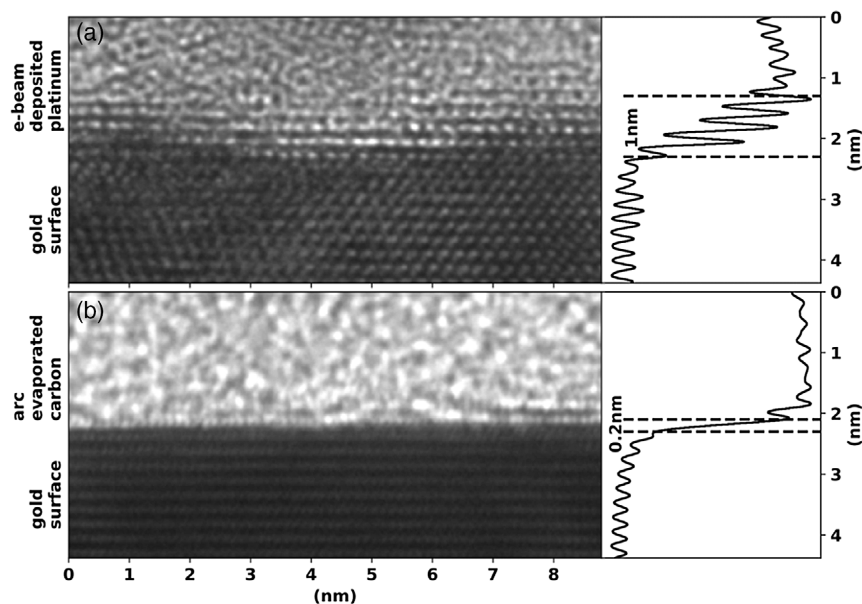

Figure 1. Comparison of the surface damage introduced with and without protective carbon coating, seen from cross-sectional HRTEM images of the gold surface of a) sample 1 at ⟨110⟩ zone axis and b) sample 2 at ⟨112⟩ zone axis. Image intensity integrated horizontally with indication of final surface roughness using evaporated carbon layer (b) and with electron deposited platinum (a).

layer. The surface of the gold samples was known to be the {111} plane and both samples were milled along the ⟨111⟩ direction. The orientation of the milling pattern relative to the crystal structure was, however, unknown, as the rotation of the crystal around the ⟨111⟩ orientation was unknown, so the available zone axis perpendicular to the ⟨111⟩ direction, within the tilting range of the sample holder, was different for the two samples. For sample 1, coated with electron beam-deposited platinum, this was a ⟨110⟩ zone axis and for sample 2, coated with arc-evaporated carbon, it was a ⟨112⟩ zone axis. Both samples show clear crystalline structure in the gold. The intensity profiles of the two images, summed along the horizontal direction, are shown to the right. In Figure 1a, the lattice fringes and mass contrast transition smoothly from the substrate to the protection layer over a distance of approximately 1 nm. As shown in Figure 1b, the transition of lattice fringes and mass contrast is sharper and transitions over a distance of approximately 0.2 nm. This difference cannot be attributed to a difference in defocus resulting in blurring, as inspection of the TEM image in Figure 1a reveals a corrugated surface rather than a gradual transition. The regions shown here are representative cutouts of larger images, showing the necessary detail. These larger images can be seen in Figure S2, Supporting Information.

The surface roughness is 4–5 atomic layers for the sample coated with electron-deposited platinum, but around one atomic layer for the sample coated with evaporated carbon. As the deposition of protective layers is not expected to flatten the surface, the greater roughness of sample 1 must be introduced during deposition of the protective layers.

Figure 2a shows an optical image of a monolayer MoS_2 flake, used to make sample 3, after exfoliation. The flake is expected to be of monolayer thickness prior to processing as the lamella was taken from a region of minimal contrast (see optical image of larger region in Figure S3, Supporting Information). The region from where the lamella was extracted based on secondary electron images acquired during FIB processing is shown in Figure S3, Supporting Information. Figure 2b shows a cross-sectional high angle annular dark field (HAADF)–STEM image of the exfoliated monolayer MoS_2 on the sputtered gold surface with evaporated carbon as the first protection layer. Figure 2c shows a vertically averaged line scan of the image intensity in the blue box in Figure 2b and an inset of the expected atomic structure of MoS_2 in the ⟨112⟩ orientation.[18] The measured intercolumn distance of 0.16 nm corresponds well to the crystal structure of MoS_2. The sample was aligned with respect to the silicon substrate crystal (see experimental details for the full sample structure), and therefore only the shown ⟨110⟩ orientation of the MoS_2 layer could be found. The good correspondence of the measured and expected atomic structure suggests that the thickness of the evaporated carbon is sufficient protection for a single monolayer of MoS_2. By comparison, sputter coating exfoliated multilayer MoS_2 with gold produces damage extending several layers deep (see Figure S5, Supporting Information). Figure 2d shows a HAADF–STEM image of multilayer MoS_2 as grown by CVD on a monocrystalline (within the feature size of a TEM lamella), gold substrate protected with evaporated carbon. As the 2D materials are grown epitaxially on the gold (111) by this process, it is possible to controllably tilt the MoS_2 layers to a ⟨110⟩ zone axis by tilting the gold substrate to a ⟨110⟩ zone axis.[19] Figure 2e shows vertically averaged line scans over the sulfur (red box in Figure 2d) and molybdenum (blue box in Figure 2d) in red and blue, respectively. The inset of the atomic structure of MoS_2 shows good agreement between the intercolumn distance of 0.26 nm and the offset of the sulfur and molybdenum columns. This shows that evaporated carbon can also protect CVD-grown MoS_2 from structural damage during

© 2020 Wiley-VCH GmbH

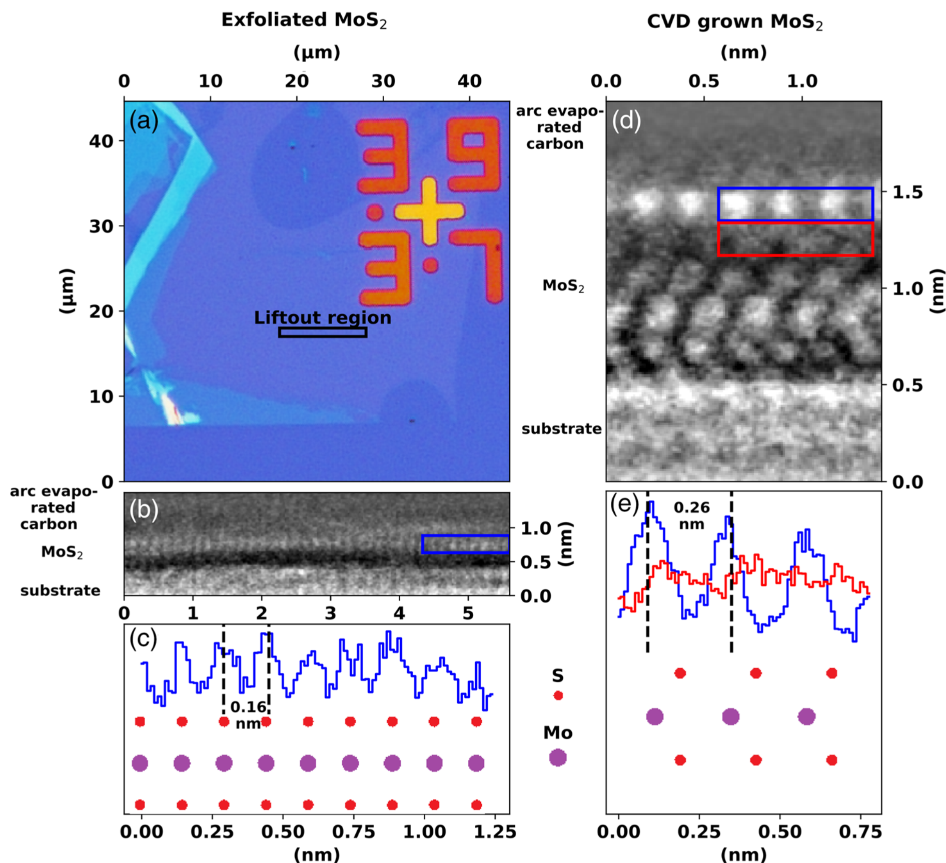

Figure 2. a) Optical micrograph of exfoliated MoS_2 (sample 3) showing color contrast corresponding to monolayer MoS_2, prior to application of protective coatings, with indication of the region where the lamellae were extracted. b) Cross-sectional STEM–HAADF image of the surface of sample 3 showing monolayer MoS_2. c) Vertically averaged image intensity from the blue box in the STEM–HAADF image above with comparison of expected position of molybdenum atoms and peaks in image intensity. d) Cross-sectional STEM–HAADF image of bilayer CVD-grown MoS_2 (sample 4). e) Vertically averaged image intensity from the blue and red box in the STEM–HAADF image above, shown as blue and red curves, respectively, with comparison of image intensity and the expected position of the sulfur and molybdenum atoms.

preparation of FIB lamellae to allow accurate characterization of the atomic structure. Cross-sectional TEM results and comparison with simulations suggest similar results for CVD-grown layers of PtS_2 (see Figure S6, Supporting Information).

Both HAADF and STEM (Figure 2b,d) images are cut out of larger images and have undergone scan noise correction and rolling background removal to highlight the position of the atomic columns due to the large difference in atomic number between gold and sulfur and final smoothening to reduce shot noise. The full original images and overview images can be seen in Figure S3, Supporting Information.

These results taken together suggest no structural damage of MoS_2, detectable by imaging, when using evaporated carbon as a protection layer. A potentially more sensitive way to test for a measurable indication of damage is the electron energy-loss spectroscopy fine structure for the sulfur atoms because they constitute the top part of the MoS_2 layer. Therefore, the sulfur $L_{2,3}$ edges is examined. **Figure 3**a shows an HAADF–STEM image of CVD-grown MoS_2 monolayer on gold coated with evaporated carbon (sample 5). The red and blue lines indicate where the electron energy loss (EEL) spectra (shown in Figure 2b) were acquired. Note that the distance between these regions is $\approx$1 nm, which is larger than the width of a single MoS_2 layer. This is done because the delocalization of the excitation would otherwise mean the EEL spectra would probe both the inner and outer sulfur layers.[20] The background subtracted and normalized electron energy loss spectroscopy (EELS) signal from the inner (blue dots) and outer (red crosses) sulfur layers are seen to be similar within noise levels. The fine structure of bulk MoS_2 (black line) (the clear pre peak at 165 eV and the weaker second peak on top of the onset of the full edge at 175 eV) is recognizable in both the outer and inner sulfur layers. These two features are different from the amorphous sulfur reference spectra supplied by Gatan, which has a smoother onset of the edge beginning at 165 eV.[21] The EEL spectra prior to background subtraction and normalization can be seen in Figure S4, Supporting Information. Note that plural scattering correction has not been performed, and thus a slight difference between the ratios of the two peaks is likely due to the sample not having the same thickness. Changes to the fine structure of the sulfur $L_{2,3}$ were therefore not detectable in monolayer MoS_2 between the outer and inner sulfur layer, and both are in agreement with a bulk MoS_2

© 2020 Wiley-VCH GmbH

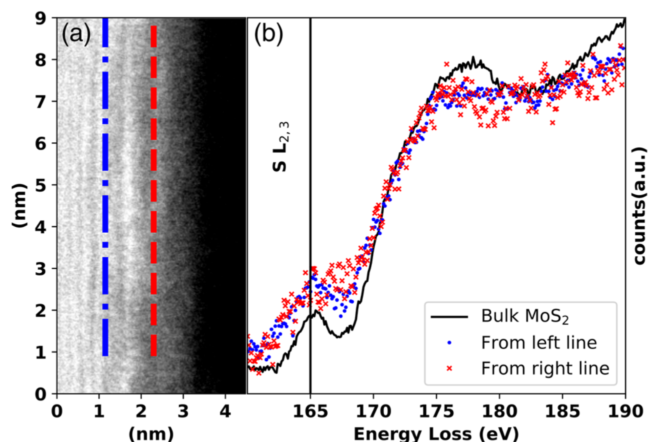

Figure 3. a) Cross-sectional STEM–HAADF image showing monolayer MoS_2 on the surface of sample 5. b) Background subtracted, normalized, and onset corrected EELS spectra acquired along the red and blue lines in the STEM–HAADF image shown as red and blue dots, respectively, and a reference spectrum (black line) from bulk MoS_2 acquired with the same microscope parameters and with the bulk crystal oriented as the monolayer MoS_2 shown to the left. The energy resolution, full width at half maximum of zero-loss peak, in the spectra is 1 eV.

reference sample with respect to the relative locations of pre-peak and edge onset.

3. Conclusion

We have examined pure gold surfaces, MoS_2 multi- and monolayers grown by CVD, and exfoliated MoS_2 monolayers in cross section, using TEM, STEM, and STEM–EELS. We have shown that evaporated carbon—in contrast to commonly used electron beam-deposited platinum—produces no detectable damage to pure gold surfaces or MoS_2 layers whether they are exfoliated or CVD grown. These results are important for the study of 2D material-based devices and for postsynthesis characterization of 2D materials. They also have important implications for FIB investigation and preparation of exposed surfaces in general. The methods described provide a simple-to-follow procedure using standard tools readily available in most laboratories equipped for SEM and TEM sample preparation, and can thus be readily applied by those working with FIB preparation and subsequent characterization of 2D materials, and sensitive exposed surfaces in general.

4. Experimental Section

Materials: Samples 1 and 2 differ only by the protective layers deposited prior to FIB milling, and otherwise consist of annealed gold on a c-plane sapphire wafer with the gold surface being the {111} plane.[19] Sample 3 exfoliated MoS_2 on gold and was made according to the methods described in ref. [22]. Samples 4 and 5 are CVD-grown MoS_2 and were made with the method described in ref. [19]. Chemically exfoliated MoS_2 samples, used for EELS reference measurements, were made with the method described by Coleman et al. using 1-methyl-2-pyrrolidinone (NMP) as the solvent.[23]

Methods: All five samples were mounted on an aluminum SEM stub using Crystal Bond and the edges were painted with silver paint to minimize charging during SE imaging and FIB milling. The FIB milling of all five samples was conducted on a FEI-Helios dual beam system operated at 5–10 kV and 0.17–5.5 nA for the electron beam and 30 kV and 28–20 000 pA for the Ga+ beam. Prior to milling the region of interest on the samples was covered with 0.2–0.5 μm electron beam-deposited platinum and 2–3 μm Ga+-deposited platinum. During the final thinning steps, the ion beam current was lowered stepwise from 280 to 26 pA during the milling. The samples were then tilted $\pm 5°$ with respect to the ion beam and polished at 2 kV and 6 pA for 10 min on both sides. Samples 2–5 were coated with carbon (Cressington Carbon 208, 60–90 s, 50–100 A) to protect the surface and subsequently sputter coated with gold (Quorum Q150T ES, 20 mA, 10 s) to further reduce charging during imaging.

TEM measurements were conducted using an image-corrected FEI Titan E-Cell 80-300 ST TEM operated at 300 kV. STEM and STEM–EELS measurements were conducted on an FEI Titan 80-300 ST TEM equipped with CESCOR preobjective lens spherical aberration corrector and a tridem 865 GIF system operated at 300 kV.

Supporting Information

Supporting Information is available from the Wiley Online Library or from the author.

Acknowledgements

A.B.A., T.B., A.S., and T.W.H. acknowledge support from the Danish National Research Foundation Center of Excellence for Nanostructured Graphene (CNG) (project DNRF103).

Conflict of Interest

The authors declare no conflict of interest.

Keywords

focused ion beam, surface damage, 2D materials, MoS_2

Received: June 16, 2020
Published online: August 13, 2020

[1] J. P. McCaffery, M. W. Phaneuf, L. D. Madsen, *Ultramicroscopy* **2001**, *87*, 97.
[2] S. Rubanov, P. R. Munroe, *J. Microsc.* **2004**, *214*, 213.
[3] S. Miroslava, S. Bernhard, Q. Ramasse, *Ultramicroscopy* **2012**, *114*, 62.
[4] L. Lan-Hsuan, Y. Chia-Hao, W. Chuan-Yu, L. Pei-Chin, H. Jih-Shang, *Ultramicroscopy* **2019**, *197*, 95.
[5] L. Chen, H. Gerlinde, C. B. Lisa, A. Rainer, *Ultramicroscopy* **2018**, *187*, 310.
[6] L. Ang-Yu, Z. Hanyu, X. Jun, C. Chih-Piao, H. Yimo, C. Ming-Hui, C. Chia-Chin, Y. Chih-Wen, W. Kung-Hwa, Y. Yiming, W. Yuan, S. Dimosthenis, N. Dennis, Y. Peidong, A. M. David, C. Mei-Yin, Z. Xiang, L. Lain-Jong, *Nat. Nanotechnol.* **2017**, *12*, 744.
[7] W. Yan, C. K. Jong, J. W. Ryan, M. Jenny, S. Xiuju, Y. Jieun, Z. Fang, M. Andre,Y. J. Hu, C. Manish, *Nature* **2019**, *568*, 70.
[8] L. Wang, I. Meric, P. Y. Huang, Q. Gao, Y. Gao, H. Tran, T. Taniguchi, K. Watanabe, L. M. Campos, D. A. Muller, J. Guo, P. Kim, J. Hone, K. L. Shepard, *Science* **2013**, *342*, 614.

 © 2020 Wiley-VCH GmbH

[9] Y. Park, B. C. Park, S. Romankov, K. J. Park, J. H. Yoo, Y. B. Lee, J. M. Yang, *J. Microsc.* **2014**, *255*, 180.
[10] S. Rubanov, P. R. Munroe, *Mater. Lett.* **2003**, *225*, 180.
[11] M. Baram, W. D. Kaplan, *J. Mircrosc.* **2008**, *232*, 395.
[12] N. I. Kato, *J. Electron Microsc.* **2004**, *53m*, 451.
[13] D. J. Barber, *Ultramicroscopy* **1993**, *52*, 101.
[14] B. W. Kempshall, L. A. Giannuzzi, B. I. Prenitzer, F. A. Stevie, S. X. Da, *J. Vac. Sci. Technol. B* **2002**, *20*, 286.
[15] S. Hata, H. Sosiati, N. Kuwano, M. Itakura, T. Nakano, Y. Umakoshi, *J. Electron Microsc.* **2006**, *55*, 23.
[16] B. An, Y. Kwon, J. Oh, Y. Shin, J. Ju, C. Yang, *Appl. Microsc.* **2019**, *49*, 6.
[17] W. Y. Kwong, W. Y. Zhang, in *ISSM 2005, IEEE Int. Symp. on Semiconductor Manufacturing*, IEEE, Piscataway, NJ **2005**, p. 469.
[18] Y. Takeuchi, W. Nowacki, *Schweiz. Mineral. Petrogr. Mitt.* **1964**, *44*, 105.
[19] A. Shivayogimath, J. D. Thomsen, D. M. A. Mackenzie, M. Geisler, R. Stan, A. J. Holt, M. Bianchi, A. Crovetto, P. R. Whelan, A. Carvalho, A. H. C. Neto, P. Hofmann, N. Stenger, P. Bøggild, T. J. Booth, *Nat. Commun.* **2019**, *10*, 2597.
[20] R. F. Egerton, *Ultramicroscopy* **2007**, *107*, 575.
[21] Gatan Inc, EELS atlas sulfur edge $L_{2,3}$ spectrum, https://eels.info/atlas/sulfur (accessed: April 2020).
[22] M. Velicky, G. E. Donnelly, W. R. Hendren, S. McFarland, D. Scullion, W. J. I. DeBenedetti, G. C. Correa, Y. Han, A. J. Wain, M. A. Hines, D. A. Muller, K. S. Novoselov, H. D. Abrun, R. M. Bowman, E. J. G. Santos, F. Huang, *ACS Nano* **2018**, *12*, 10463.
[23] J. N. Coleman, M. Lotya, A. O'Neill, S. D. Bergin, P. J. King, U. Khan, K. Young, A. Gaucher, S. De, R. J. Smith, I. V. Shvets, S. K. Arora, G. Stanton, H. Kim, K. Lee, G. T. Kim, G. S. Duesberg, T. Hallam, J. J. Boland, J. J. Wang, J. F. Donegan, J. C. Grunlan, G. Moriarty, A. Shmeliov, R. J. Nicholls, J. M. Perkins, E. M. Grieveson, K. Theuwissen, D. W. McComb, P. D. Nellist, V. Nicolosi, *Science* **2011**, *331*, 568.

© 2020 Wiley-VCH GmbH